Statistical analysis

All analyses were conducted on four ultrametric trees (Langley–Fitch and NPRS branch lengths for both the maximum-likelihood and bayesian phylogenies); further analyses were run assuming both a speciational and a gradual mode of character evolution. Results from these analyses were qualitatively nearly identical.

To examine whether distances between species in ecological space was related to phylogenetic proximity, we conducted a Mantel test comparing matrices of ecological and phylogenetic distance. Ecological distance was the euclidean distance between species in a multidimensional space determined by the axes of a PC analysis. Phylogenetic distances were the branch lengths separating species (that is, their patristic distance). To examine whether niche position of the species in the two species-rich clades (Fig. 1) was conserved, we examined whether members of these clades occupied a nonrandomly small part of ecological space relative to the other species by conducting a MANOVA with PC axis scores as variables and five groups (the two clades and the other three species).

Then, to assess whether members of these clades were more similar to each other than would be expected by random evolutionary divergence, we calculated for each clade the ratio of the mean distance between species within the clade and the mean distance of species within the clade to other species. To assess whether these ratios were unusually small, we conducted phylogenetic simulations. For each significant PC axis, trait evolution was simulated on the phylogeny assuming either gradual or speciational models of character evolution; variance in trait value among species in the simulations was adjusted to that observed in the real data. Using these simulations, we then assessed whether the ratios for each clade separately or for the average of the two clades was significantly smaller than expected by chance.

To determine whether species were nonrandomly dispersed in ecological space, we examined whether the pairwise euclidean distance between species on one PC axis was negatively related to the distance along a second axis ('niche complementarity'). Because the three pairwise comparisons among the three PC axes are not independent, an experiment-wise P-value cannot be calculated. We investigated the statistical significance of these findings using phylogenetic simulation as above. For both the real and simulated values, correlations were calculated between euclidean distances on each possible pairwise combination of PC axis scores.

1. Peterson, A. T., Soberón, J. & Sánchez-Cordero, V. Conservatism of ecological niches in evolutionary time. *Science* **285**, 1265–1267 (1999).
2. Prinzing, A., Durka, S., Klotz, W. & Brandl, R. The niche of higher plants: evidence for phylogenetic conservatism. *Proc. R. Soc. Lond. B* **268**, 2383–2389 (2001).
3. Webb, C. O., Ackerly, D. D., McPeek, M. A. & Donoghue, M. J. Phylogenies and community ecology. *Annu. Rev. Ecol. Syst.* **33**, 475–505 (2002).
4. Harvey, P. H. & Pagel, M. D. *The Comparative Method in Evolutionary Biology* (Oxford Univ. Press, Oxford, 1991).
5. MacArthur, R. H. *Geographical Ecology* (Princeton Univ. Press, Princeton, 1972).
6. Schluter, D. *The Ecology of Adaptive Radiation.* (Oxford Univ. Press, Oxford, 2000).
7. Silvertown, J., Dodd, M. & Gowing, D. Phylogeny and the niche structure of meadow plant communities. *J. Ecol.* **89**, 428–435 (2001).
8. Losos, J. B. Integrative approaches to evolutionary ecology: *Anolis* lizards as model systems. *Annu. Rev. Ecol. Syst.* **25**, 467–493 (1994).
9. Roughgarden, J. *Anolis Lizards of the Caribbean: Ecology, Evolution, and Plate Tectonics* (Oxford Univ. Press, 1995).
10. Jackman, T. R., Larson, A., de Queiroz, K. & Losos, J. B. Phylogenetic relationships and tempo of early diversification in *Anolis* lizards. *Syst. Biol.* **48**, 254–285 (1999).
11. Schoener, T. W. & Schoener, A. Densities, sex ratios, and population structure in four species of Bahamian *Anolis* lizards. *J. Anim. Ecol.* **49**, 19–53 (1980).
12. Reagan, D. P. Congeneric species distribution and abundance in a three-dimensional habitat: the rain forest anoles of Puerto Rico. *Copeia*, **1992**, 392–403 (1992).
13. Leal, M., Rodríguez-Robles, J. A. & Losos, J. B. An experimental study of interspecific interactions between two Puerto Rican *Anolis* lizards. *Oecologia* **117**, 273–278 (1998).
14. Losos, J. B. & Spiller, D. Differential colonization success and asymmetrical interactions between two lizard species. *Ecology* **80**, 252–258 (1999).
15. Gerber, G. P. & Echternacht, A. C. Evidence for asymmetrical intraguild predation between native and introduced *Anolis* lizards. *Oecologia* **124**, 599–607 (2000).
16. Schoener, T. W. Resource partitioning in ecological communities. *Science* **185**, 27–39 (1974).
17. Darwin, C. *On the Origin of Species* Ch. 3 (Murray, London, 1859).
18. Hutchinson, G. E. *The Ecological Theater and the Evolutionary Play* Ch. 2 (Yale Univ. Press, New Haven, 1965).
19. Petren, K., Grant, B. R. & Grant, P. R. A phylogeny of Darwin's finches based on microsatellite DNA length variation. *Proc. R. Soc. Lond. B* **266**, 321–329 (1999).
20. Danley, P. D. & Kocher, T. D. Speciation in rapidly diverging systems: lessons from Lake Malawi. *Mol. Ecol.* **10**, 1075–1086 (2001).
21. Richman, A. D. & Price, T. Evolution of ecological differences in the Old World leaf warblers. *Nature* **355**, 817–821 (1992).
22. Butler, M. A. & Losos, J. B. Multivariate sexual dimorphism, sexual selection, and adaptation in Greater Antillean *Anolis* lizards. *Ecol. Monogr.* **72**, 541–559 (2002).
23. Swofford, D. *PAUP*: Phylogenetic Analysis Using Parsimony (*and Other Methods)* (Sinauer, Sunderland, MA, 2000).
24. Huelsenbeck, J. P. & Ronquist, F. MRBAYES: Bayesian inference of phylogeny. *Bioinformatics* **17**, 754–755 (2001).
25. Posada, D. & Crandall, K. A. Modeltest: testing the model of DNA substitution. *Bioinformatics* **14**, 817–818 (1998).
26. Langley, C. H. & Fitch, W. An estimation of the constancy of the rate of molecular evolution. *J. Mol. Evol.* **3**, 161–177 (1974).
27. Rodríguez Schettino, L. *The Iguanid Lizards of Cuba* (Univ. Press Florida, Gainesville, 1999).
28. Macey, J. R. *et al.* Phylogenetic relationships among agamid lizards of the *Laudakia caucasia* species group: testing hypotheses of biogeographic fragmentation and an area cladogram for the Iranian Plateau. *Mol. Phylogenet. Evol.* **10**, 118–131 (1998).
29. Shochat, D. & Dessauer, H. C. Comparative immunological study of albumins of *Anolis* lizards of the Caribbean islands. *Comp. Biochem. Physiol.* **68A**, 67–73 (1981).
30. de Queiroz, K., Chu, L.-R. & Losos, J. B. A second *Anolis* lizard in Dominican amber and the systematics and ecological morphology of Dominican amber anoles. *Am. Mus. Nat. Hist. Novitates* **3249**, 1–23 (1998).

Constrained circulation at Endeavour ridge facilitates colonization by vent larvae

Richard E. Thomson[1], **Steven F. Mihály**[1], **Alexander B. Rabinovich**[1,2], **Russell E. McDuff**[3], **Scott R. Veirs**[3] & **Frederick R. Stahr**[3]

[1]*Institute of Ocean Sciences, 9860 West Saanich Road, Sidney, British Columbia, V8L 4B2, Canada*
[2]*P.P. Shirshov Institute of Oceanology, Moscow 117851, Russia*
[3]*School of Oceanography, University of Washington, Seattle, Washington 98195-7940, USA*

....

Understanding how larvae from extant hydrothermal vent fields colonize neighbouring regions of the mid-ocean ridge system remains a major challenge in oceanic research[1,2]. Among the factors considered important in the recruitment of deep-sea larvae are metabolic lifespan, the connectivity of the seafloor topography, and the characteristics of the currents[3]. Here we use current velocity measurements from Endeavour ridge to examine the role of topographically constrained circulation on larval transport along-ridge. We show that the dominant tidal and wind-generated currents in the region are strongly attenuated within the rift valley that splits the ridge crest, and that hydro-thermal plumes rising from vent fields in the valley drive a steady near-bottom inflow within the valley. Extrapolation of these findings suggests that the suppression of oscillatory currents within rift valleys of mid-ocean ridges shields larvae from cross-axis dispersal into the inhospitable deep ocean. This effect, augmented by plume-driven circulation within rift valleys having active hydrothermal venting, helps retain larvae near their source. Larvae are then exported preferentially down-ridge during regional flow events that intermittently over-ride the currents within the valley.

The Endeavour segment of Juan de Fuca ridge (Endeavour ridge) is a hydrothermally active, intermediate-rate spreading centre located in 2,500 m of water roughly 300 km seaward of British Columbia and Washington State in the northeast Pacific (Fig. 1). Hydrothermal venting from this segment is concentrated within a 1-km-wide, 10-km-long rift valley located along the ridge crest. Water depths within the axial valley shoal from 2,300 m in the south to 2,170 m in the north. Valley relief ranges from 100 to 150 m. A 25-km-wide, 50-km-long depression links the southern end of the Endeavour segment to the main portion of Juan de Fuca ridge.

letters to nature

(Topographic maps for Juan de Fuca ridge are available at http://ocean-ridge.ldeo.columbia.edu/ne_pac/imagery/imag_gif/nep112m.gif) The five major vent fields at Endeavour ridge are spaced 2–3 km apart along the axial rift valley[4], with the apparently younger, highly active fields (Mothra, Main Endeavour, High Rise) located in the southern sector, and the older, weakly active fields (Salty Dawg, Sasquatch) located in the northern sector. The Main Endeavour field alone generates a total heat flux of 650 ± 100 megawatts (MW) through a combination of focused, high-temperature (350 °C) venting and diffuse, low-temperature (10–25 °C) venting[5]. Vent plumes—as defined by their thermal, particulate and chemical anomalies—rise to a level of neutral buoyancy 50–350 m above bottom. Deeper portions of the plumes can remain trapped within the valley whereas those rising above the ridge crests are free to drift with the ambient flow.

Currents at Endeavour ridge and over the deep off-ridge site to the north (Fig. 1) consist of zero-mean oscillatory currents with amplitudes of about $10\,\mathrm{cm\,s}^{-1}$ superimposed on a near-steady background flow of about $5\,\mathrm{cm\,s}^{-1}$. Oscillatory currents are in five primary frequency bands: (1) The semidiurnal band, principally the M_2 and S_2 tidal constituents with periods of 12.4 and 12.0 h, respectively; (2) the diurnal band, principally the K_1 and O_1 tidal constituents with periods of 23.9 and 25.8 h, respectively; (3) the wind-forced inertial (f) band with periods of approximately 16 h (frequencies a few per cent above the local Coriolis frequency, $f \approx 1.08 \times 10^{-4}\,\mathrm{s}^{-1}$); (4) the low-frequency 'weather' band spanning periods of days to weeks, with a broad spectral peak in the range of 4 to 6 days[6]; and (5) the high-frequency band arising mainly from nonlinear interactions among inertial and tidal frequencies[7]. Tidal currents account for roughly 50% of the flow variance.

The predominant M_2 tidal currents are aligned along-ridge (direction of strike $\approx 20°$ true) with major tidal ellipse axes diminishing from about $5\,\mathrm{cm\,s}^{-1}$ above the ridge crest to 2–$3\,\mathrm{cm\,s}^{-1}$ within the confines of the valley (Fig. 2). The predominant K_1 diurnal tidal currents are oriented cross-axis above the ridge, become increasingly clockwise rotary with proximity to the ridge crest, and then aligned along-axis within the axial valley. Diurnal currents are amplified by a factor of 3–4 at the ridge crest but are attenuated to $1\,\mathrm{cm\,s}^{-1}$ within the valley. Intermittent (roughly 1-week duration), wind-forced, inertial currents—often the strongest type of flow in the deep ocean—attain speeds of about $5\,\mathrm{cm\,s}^{-1}$ immediately above the ridge crest but are annihilated within the confines of the valley. Similarly, low-frequency currents within the wind-forced synoptic band are amplified by as much as a factor of seven near the ridge crest[8], but are strongly damped within the valley.

Current meter data from 2000 and 2001, along with current records collected in the 1980s and 1990s, indicate a two-tier mean flow structure at Endeavour ridge (Fig. 3). Immediately above the ridge crest (Fig. 3a, top panel), and at elevations exceeding approximately 75–100 m above the valley floor (Fig. 3b, c), the slowly varying background flow is roughly along-axis towards the southwest and often exceeds $5\,\mathrm{cm\,s}^{-1}$. However, periods of cross-axis velocity are common and often linked to eddy-like circulation (Fig. 3b). As one descends into the valley, the speed of the along-ridge current decreases and the flow becomes persistently into the valley. This 'inflow' draws cold bottom water towards the central buoyancy sources and is strongest (about $5\,\mathrm{cm\,s}^{-1}$) in the southern and central sectors of the valley (Fig. 3c), where the valley is deepest and hydrothermal outputs are the highest. Inflow is weakest (about $1\,\mathrm{cm\,s}^{-1}$) at the northern end, where the valley is shallowest and hydrothermal output is lowest. The shallow topographic saddle at the northern end of the valley, combined with the much higher thermal outputs from the southern and central vent fields, may explain why northward inflow extends well into the central valley from the south. Although the inflow is remarkably steady, it stalls or reverses direction (roughly 10% of the time at the central mooring

site) during intermittent bursts of strong southwesterly flow in the overlying water column. In autumn and winter, reversals occur every few weeks (Fig. 3a, lower panel) and persist for one or two days with along-axis flow speeds of 5 to $10\,\mathrm{cm\,s}^{-1}$.

We can generalize our observations to other sectors of the global mid-ocean ridge system. Specifically, the ubiquitous diurnal tidal currents and wind-generated inertial currents of the deep ocean become amplified and more circularly polarized above the crests and flanks of oceanic ridges. If we view these amplified currents as turbulent-like fluctuations superimposed on a slowly varying mean flow, it follows that there is pronounced cross-axis dispersion of passively drifting larvae above oceanic ridge crests. (Here, dispersion arises from random velocity fluctuations, as well as from heterogeneity in the tidal and inertial flow fields.) Even if these topographically enhanced current speeds diminish slowly as L^{-1}
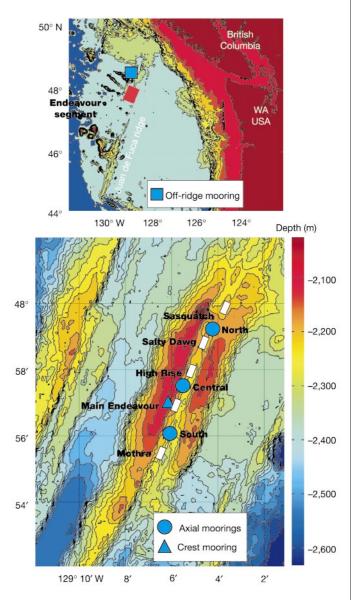

Figure 1 Chart of Endeavour ridge with an expanded view of the axial valley region. Small rectangles denote the five major vent sites within the valley. Circles denote the valley sites for the south mooring in the summer of 2000 and north, central and south moorings in the summer of 2001. The triangle denotes the 1996–97 bottom mooring site on the western ridge crest; the square in the top panel shows the off-ridge mooring site for 2000. Depth scale in metres applies to the lower panel.

away from the ridge crest ($L \approx 10$ km is the ridge width), dispersion is still sufficient to transport larvae well away from the ridge into the inhospitable deep ocean. This enhanced cross-axis dispersion by bottom-intensified oscillatory currents above ridge crests presumably carries vent larvae beyond the influence of transport by along-ridge mean currents, regardless of how they are formed. Therefore, despite its obvious appeal, the concept that mean along-axis currents above the ridge crest are the primary factor in successful larval colonization is unlikely.

Contrary to the situation above the ridge crest, oscillatory currents within axial valleys (in the case of slow- and intermediate-spreading regions) or summit grabens (in the case of fast-spreading regions) can be strongly attenuated and rectified by the steep topography. Flow attenuation and rectification increase the likelihood for successful downstream recruitment by creating a volume of water that is sheltered from off-ridge transport. This effect will be augmented by plume-induced inflow for hydrothermally active rift valleys. Plume-induced inflow (Fig. 4) would facilitate the aggregation of vent larvae in the water column near their source region before their export downstream. Larvae with negative buoyancy relative to water above the ridge crest would presumably sink back into the valley should they become swept upward in a plume. These larvae will tend to remain within the valley, just as large (5 μm diameter) mineral particles tend to be vertically recycled in hydrothermal plumes if they are not advected more than a few kilometres from their source[9]. On the other hand, larvae with positive buoyancy will rise or remain above the ridge crest where they are susceptible to cross-ridge dispersion. For vent organisms such as the tubeworm *Riftia pachyptila*—whose mean lifespan away from the source region is only about 38 days[3]—

successful transport to an adjacent ridge segment by the mechanism proposed here is most likely to occur during along-ridge flow events that intermittently over-ride the circulation within the valley. Regional large-scale flow events would 'flush' the larvae along the ridge axis, the direction most favourable for recruitment. For larvae transported to the vicinity of newly formed vent fields, the presence of recently established plume-induced inflow may facilitate recruitment to the new habitat.

Because steep walls attenuate oscillatory currents over a broad frequency range, rift valleys and escarpments provide stepping stones or conduits for the along-ridge transport of vent-derived products. Intermittent regional flow events then provide the vehicle for rapid and directed transport of vent larvae to distant vent fields. At present, there are too few velocity data for the global mid-ocean ridge system for us to confirm the general applicability of our circulation-based model. However, we can speculate that segment-to-segment colonization by larvae is most successful for

Figure 3 Daily mean current vectors. **a**, West ridge site, June 1996 to July 1997, and the central valley site from June 1999 to May 2000; **b**, the five current meter depths at the south mooring site in year 2000; and **c**, current meters at the north, central and south sites in year 2001. Labels give instrument depth above bottom. North is upward in all figures. Vectors point in the direction of flow. The bottom panel in **a** shows numerous periods of flow reversal within the axial valley.
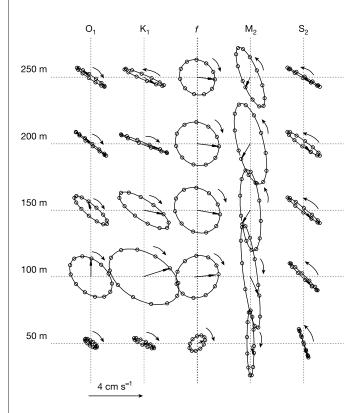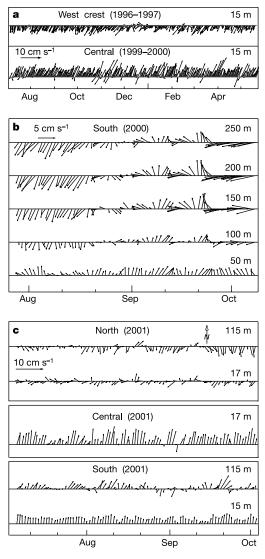

Figure 2 Current ellipses and vectors for the four major tidal constituents and inertial currents (*f*) for all five depths for the south mooring site in the year 2000. Numbers give instrument depth above bottom. Vectors denote currents at an initial time, t_0. Small circles mark time steps for the current vectors; arrows outside the ellipse denote the direction of vector rotation. Along-axis is upward in all figures.
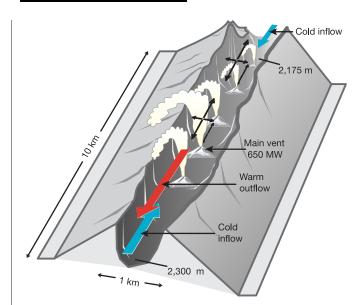
Figure 4 Diagram of the dominant flow within the axial valley of Endeavour ridge. High-frequency oscillatory currents are amplified over the ridge crest (back-and-forth current vectors) but suppressed and rectified within the confines of the valley. Mean background currents carry plume water to the southwest above the ridge crest whereas plume-induced currents transport cold ambient water into the valley below about 75 m elevation. Strongest inflow occurs at the southern end of the valley. Venting dissipates about 1,500 MW, with 650 MW from the Main Endeavour Field alone. Plume sizes are roughly proportional to thermal outputs from the five vent fields.

intermediate-spreading ridges (such as Juan de Fuca ridge), where segments are relatively close together and contain active hydrothermal vent fields in well-defined axial valleys. We further speculate that there is significant colonization success for fast-spreading ridges (such as the East Pacific Rise), where rift valleys are shallower (about 10 m) but more continuous (about 100 km). Possibly less conducive to colonization are the rift valleys of slow-spreading ridges (such as the Mid-Atlantic Ridge) where numerous fracture zones, transform off sets, and large silled valleys can break up ridge segments[10]. Major breaks in ridge segments may isolate vent organisms unless the large-scale ocean circulation is predominantly along-ridge. On a geological timescale, our findings imply that periods of enhanced ridge building and associated hydrothermal venting are periods of reduced biogeographic diversity whereby vent larvae are distributed more readily along crests of the global ridge system, and vice versa. Regardless of which processes predominate, our findings strongly express the need for detailed current measurements in any study investigating the dispersion and colonization of vent fauna within the global ridge system. □

Methods

Moored current-meter observations

Current meters were moored 15–17 m above bottom on the west ridge crest from June 1996 to July 1997, near the Main (central) Endeavour Field from June 1999 to May 2000, and at three sites along the axial valley in 2001 (Fig. 1). A single string of five current meters at 50-m depth increments was deployed near the main field from July to October 2000. The latter provides high vertical resolution of the flow in the central valley whereas the former provides reasonably high along-ridge resolution of the flow within the valley.

An empirical model of plume-driven circulation

As proposed for segments of the Mid-Atlantic Ridge[11], it is feasible that enhanced diapycnal mixing over the rough topography of the axial valley is a primary cause for the intensified, unidirectional background flow we observed within the south-central portion of the axial valley. However, given the widespread extent of vigorous hydrothermal venting within the valley and observational evidence that the inflow is confined below the base of the neutrally buoyant plumes, it is more likely that the inflow is a dynamic response to the

turbulent entrainment of cold (2 °C) ambient bottom water by plumes rising from superheated (350 °C) and low-temperature (10–25 °C) vent sources. This explanation becomes even more compelling if one examines conservation of fluid mass. Specifically, buoyant plumes rising from the major hydrothermal vent fields located within the southern sector of the valley entrain approximately 5,000 times the mass of the source waters exiting the vent orifices by the time they reach their level of neutral buoyancy[12]. Roughly 40% of this entrainment occurs within the first 75 m of rise, well within the confines of the valley. The vertical flux of fluid mass, Q_V, at 75 m elevation is then related to the vertical flux of mass, Q_S, from the bottom sources through the relation

$$Q_V = (0.4)5,000Q_S \qquad (1)$$

To support this entrainment, fluid must enter at the ends of the axial valley, particularly from the deeper, more hydrothermally active southern end of the valley. Our observations show that the mean inflow at the southern end of the valley, v_S, is about four times the mean inflow at the northern end, v_N. Thus, by mass conservation

$$Q_V \approx 1.25Av_S \qquad (2)$$

where A ($\approx 40 \times 10^3$ m^2) is the cross-sectional area of the valley up to an elevation of 75 m. The recent estimate of about 650 ± 100 MW for the heat flux for the Main Endeavour Field[13] (which is larger than previous estimates of about 340 MW[14,15]) indicates that the main field contributes approximately 40% of the total heat flux $F_S \approx 1,500$ MW for the ridge segment. (Segment scale estimates for Endeavour ridge[16–18] range from 1,000 to 3,000 MW.) Relating the mass flux of the segment sources to the corresponding heat flux gives

$$Q_S \approx F_S/\rho C_P \Delta\theta \qquad (3)$$

where $\rho C_P \approx 4.3 \times 10^6$ J K^{-1} m^{-3} is the heat capacity per unit mass for water and $\Delta\theta \approx 350$ °C is the typical temperature contrast between vent fluids and the ambient water. Solving equations (1) to (3) for the mean inflow, v_S, at the southern end of the valley yields

$$v_S \approx \frac{(0.4)5,000F_S}{1.25A\rho C_P \Delta\theta} \approx \frac{(0.4)5,000 \times 1500 \times 10^6 \text{ J s}^{-1}}{(1.25)(4 \times 10^4 \text{ m}^2)(4.3 \times 10^6 \text{ J K}^{-1} \text{ m}^{-3})350 \text{ K}} \approx 4 \text{ cm s}^{-1}$$

The plume-induced inflow at the northern end of the valley is then $v_N \approx 1$ cm s^{-1}. Our estimates for v_S and v_N become almost identical with observed background currents at their respective ends of the valley if we account for the fact that inflows are typically offset by a southward regional current of 1–2 cm s^{-1}.

One study observed a deep (>3,010 m depth) influx $Q_U = 5.30 \pm 0.55 \times 10^3$ m^3 s^{-1} within a 50-km-long, silled segment of the Mid-Atlantic Ridge at 29° N but provided no mechanistic link between the flux and the 275-MW output from hydrothermal vent fields contained within the valley[10]. However, if we assume that the valley has $N = 10$ vent sites, each having a surface area $A = 0.03$ m^2, plume exit velocities of $w = 1$ m s^{-1}, and a dilution factor of 7,500:1 (ref. 19), we obtain a vertical flux of entrained fluid $Q_V = NAw7,500 = 2.25 \times 10^3$ m^3 s^{-1}, about 40% of the observed value, Q_U. Thus, thermal buoyancy effects may also be contributing to the deep inflow at this segment of the Mid-Atlantic Ridge.

1. Tunnicliffe, V. The biology of hydrothermal vents: Ecology and evolution. *Oceanogr. Mar. Biol. Ann. Rev.* **29**, 319–407 (1991).
2. van Dover, C. L., German, C. R., Speer, K. G., Parson, L. M. & Vrijenhoek, R. C. Evolution and biogeography of deep-sea vents and seep invertebrates. *Science* **295**, 1253–1257 (2002).
3. Marsh, A. G., Mullineaux, L. S., Young, C. M. & Manahan, D. T. Larval dispersal potential of the tubeworm *Riftia pachyptila* at deep-sea hydrothermal vents. *Nature* **411**, 77–80 (2001).
4. Kelley, D. S., Delaney, J. R. & Lilley, M. D. Vent field distribution and evolution along the Endeavour segment, Juan de Fuca Ridge. *EOS Trans. AGU* **82** 47, F612 (2001).
5. Stahr, F. R., McDuff, R. E., Yoerger, D. R., Bradley, A. M. & Nakamura, K. Heat flux measurements at the Main Endeavour vent field. Juan de Fuca Ridge. *Eos Trans. AGU* (Fall Mtg Suppl. Abstr) **81**(48), (2000) OS52I-03.
6. Cannon, G. A. & Thomson, R. E. Characteristics of a 4-day oscillation trapped by the Juan de Fuca Ridge. *Geophys. Res. Lett.* **23**, 1613–1616 (1996).
7. Mihaly, S. F., Thomson, R. E. & Rabinovich, A. B. Evidence for nonlinear interaction between internal waves of inertial and semidiurnal frequency. *Geophys. Res. Lett.* **25**, 1205–1208 (1998).
8. Lavelle, J. W. & Cannon, G. A. On subinertial oscillations trapped by the Juan de Fuca Ridge, northeast Pacific. *J. Geophys. Res.* **106**, 31099–31116 (2001).
9. German, C. R. & Sparks, R. S. J. Particle recycling in the TAG hydrothermal plume. *Earth Planet. Sci. Lett.* **116**, 129–134 (1993).
10. Murton, B. J., Redbourn, L. J., German, C. R. & Baker, E. T. Sources and fluxes of hydrothermal heat, chemicals and biology within a segment of the Mid-Atlantic Ridge. *Earth Planet. Lett.* **171**, 301–317 (1999).
11. Thurnherr, A. M., Richards, K. J., German, C. R., Lane-Serff, G. F. & Speer, K. G. Flow and mixing in the Rift Valley of the Mid-Atlantic Ridge. *J. Phys. Oceanogr.* **32**, 1763–1778 (2002).
12. McDuff, R. E. in *Physical, Chemical, Biological, and Geological Interactions within Seafloor Hydrothermal Systems* (eds Humphris, S. E., Zierenberg, R. A., Mullineaux, L. S. & Thomson, R. E.) 357–368 (American Geophysical Union Monograph, Washington, 1995).
13. Veirs, S. R. *Heat Flux and Hydrography at a Submarine Volcano: Observations and Models of the Main Endeavour Vent Field in the Northeast Pacific* PhD thesis, Univ. Washington (2003).
14. Bemis, K. G., von Herzen, R. P. & Mottl, M. J. Geothermal heat flux from hydrothermal plume on the Juan de Fuca Ridge. *J. Geophys. Res.* **98**, 6351–6369 (1993).
15. Ginster, U., Mottl, M. J. & von Herzen, R. P. Heat flux from black smokers on the Endeavour and Cleft segments, Juan de Fuca Ridge. *J. Geophys. Res.* **99**, 4937–4950 (1994).
16. Baker, E. T. & Massoth, G. J. Characteristics of hydrothermal plumes from two vent fields on the Juan de Fuca Ridge, northeast Pacific Ocean. *Earth Planet. Sci. Lett.* **85**, 59–73 (1987).

17. Rosenberg, N. D. *et al.* Estimation of heat and chemical fluxes from a seafloor hydrothermal vent field using radon measurements. *Nature* **334,** 604–607 (1988).
18. Thomson, R. E., Delaney, J. R., McDuff, R. E., Janecky, D. R. & McClain, J. S. Physical characteristics of the Endeavour Ridge hydrothermal plume during July 1988. *Earth Planet. Sci. Let.* **111,** 141–154 (1992).
19. Lupton, J. E., Delaney, J. R., Johnson, H. P. & Tivey, M. K. Entrainment and vertical transport of deep-ocean water by buoyant hydrothermal plumes. *Nature* **316,** 621–623 (1985).

....

Evolutionary capacitance as a general feature of complex gene networks

Aviv Bergman[1,2] **& Mark L. Siegal**[1]

[1] *Department of Biological Sciences, Stanford University, Stanford, California 94305-5020, USA*
[2] *Center for Computational Genetics and Biological Modeling, Stanford University, Stanford, California 94305-5020, USA*

....

An evolutionary capacitor buffers genotypic variation under normal conditions, thereby promoting the accumulation of hidden polymorphism. But it occasionally fails, thereby revealing this variation phenotypically[1]. The principal example of an evolutionary capacitor is Hsp90, a molecular chaperone that targets an important set of signal transduction proteins. Experiments in *Drosophila* and *Arabidopsis* have demonstrated three key properties of Hsp90: (1) it suppresses phenotypic variation under normal conditions and releases this variation when functionally compromised; (2) its function is overwhelmed by environmental stress; and (3) it exerts pleiotropic effects on key developmental processes[1,2]. But whether these properties necessarily make Hsp90 a significant and unique facilitator of adaptation[1–10] is unclear. Here we use numerical simulations of complex gene networks, as well as genome-scale expression data from yeast single-gene deletion strains, to present a mechanism that extends the scope of evolutionary capacitance beyond the action of Hsp90 alone. We illustrate that most, and perhaps all, genes reveal phenotypic variation when functionally compromised, and that the availability of loss-of-function mutations accelerates adaptation to a new optimum phenotype. However, this effect does not require the mutations to be conditional on the environment. Thus, there might exist a large class of evolutionary capacitors whose effects on phenotypic variation complement the systemic, environment-induced effects of Hsp90.

Several studies on other genes than that encoding Hsp90 have also reported increased phenotypic variance in mutant strains[11,12]. These results have been taken as evidence that wild-type organisms are buffered, or 'canalized', against environmental and genetic variation[13]. We previously demonstrated that canalization does not require a dedicated mechanism (such as that provided by chaperone proteins), but instead arises as an emergent property of complex developmental–genetic networks that reach a steady state

of gene expression[14]. We therefore proposed that a loss of buffering might be induced by compromising the function of an evolved network, namely by removing the function of an arbitrary gene in the network. To test this hypothesis, we use simulations of gene networks and ask how an arbitrary null ('knockout') mutation affects the expression of other genes. Does a network with a single gene knocked out exhibit a greater range of phenotypes, across environmental conditions or genetic backgrounds, than does the wild-type network from which it was derived? If so, the knocked-out gene has the potential to be an evolutionary capacitor.

First we consider the effect of knockouts in different genetic backgrounds. We use a representation of a gene network in which each of N genes produces a factor that is capable of influencing the expression of each other gene as well as itself[14,15] (see Fig. 1 and Supplementary Information; $N = 10$ for all simulations presented here). An $N \times N$ matrix encapsulating the regulatory relationships is considered the 'genotype' of an individual. Unlike standard quantitative-genetic and population-genetic frameworks, this representation lends itself to the study of developmental buffering, because development is explicitly modelled as the progression from an initial gene-expression state to a state of gene-expression equilibrium. The equilibrium gene-expression profile is considered to be the 'phenotype', and those genotypes that do not produce an equilibrium state are considered lethal (see refs 14 and 15 for a justification of this definition of lethality). A knockout of a gene is represented by zeroing the corresponding row and column of the regulatory matrix.

To study a population of individuals that differ in genotype but, for the most part, have the same phenotype, we perform 100 evolutionary simulations in which a randomly generated, non-lethal individual founds a population of size 500 that is allowed to evolve, with mutation of the elements of the regulatory matrix, for 400 generations. During evolution there is strong selection both against lethal disruptions in gene-expression equilibrium and for the phenotype of the founder individual, as described previously[14]. Setting the founder's phenotype as optimal in this way ensures that the range of phenotypes in the final population of 500 individuals at generation 400 is very narrow, thus permitting comparison with the range of phenotypes seen in the knockout derivatives of each of the 500 individuals. Out of 1,000 such comparisons (100 simulations × 10 gene knockouts), only 4 showed higher phenotypic variation for the wild-type population than for its knockout derivatives ($P \approx 0$, sign test; for a detailed analysis see Supplementary Information). Results of a typical simulation are shown in
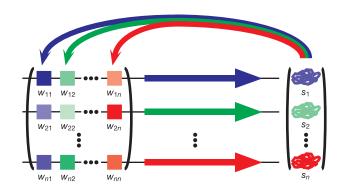

Figure 1 Representation of a gene network. Each gene (horizontal arrow) is regulated by the products of the other genes by means of upstream enhancer elements (boxes). The strength and direction of regulation (depicted as different colour saturation levels) are a function of both the regulatory element and the abundance of its corresponding gene product. Genotype is represented as the matrix, W, of regulatory interactions, and phenotype is the vector, $\hat{S}$, of gene-product levels at equilibrium.